Editors' Suggestion

Gate-tunable kinetic inductance parametric amplifier

Lukas Johannes Splitthoff,[1,2,*] Jaap Joachim Wesdorp,[1,2] Marta Pita-Vidal,[1,2] Arno Bargerbos,[1,2] Yu Liu,[3] and Christian Kraglund Andersen[1,2]

[1] *QuTech, Delft University of Technology, 2628 CJ Delft, Netherlands*
[2] *Kavli Institute for Nanoscience, Delft University of Technology, 2628 CJ Delft, Netherlands*
[3] *Center for Quantum Devices, Niels Bohr Institute, University of Copenhagen, 2100 Copenhagen, Denmark*

(Received 20 August 2023; revised 29 October 2023; accepted 18 December 2023; published 25 January 2024)

Superconducting parametric amplifiers play a crucial role in the preparation and readout of quantum states at microwave frequencies, enabling high-fidelity measurements of superconducting qubits. Most existing implementations of these amplifiers rely on the nonlinearity from Josephson junctions, superconducting quantum interference devices, or disordered superconductors. Additionally, frequency tunability arises typically from either flux or current biasing. In contrast, semiconductor-based parametric amplifiers are tunable by local electric fields, which impose a smaller thermal load on the cryogenic setup than current and flux biasing and lead to vanishing crosstalk to other on-chip quantum systems. In this work, we present a gate-tunable parametric amplifier that operates without Josephson junctions, using a proximitized semiconducting nanowire. This design achieves near-quantum-limited performance, featuring more than 20-dB gain and a 30-MHz gain-bandwidth product. The absence of Josephson junctions results in advantages, including substantial saturation powers of −120 dBm, magnetic field compatibility up to 500 mT, and frequency tunability over a range of 15 MHz. Our realization of a parametric amplifier supplements efforts towards gate-controlled superconducting electronics, further advancing the abilities for high-performing quantum measurements of semiconductor-based and superconducting quantum devices.

DOI: 10.1103/PhysRevApplied.21.014052

I. INTRODUCTION

In the pursuit of advancing quantum technologies, the extraction and amplification of weak quantum signals have emerged as crucial challenges in all known qubit platforms, especially those operating in cryogenic environments. The amplification chains required for weak signals must be carefully designed to exhibit specific characteristics, including high gain, wide amplification bandwidth, and large saturation power, while maintaining minimal added noise, to maximize the signal-to-noise ratio (SNR) for high-performing readout [1–3]. Superconducting parametric amplifiers (PAs) based on Josephson junctions already play a pivotal role in the first stage of amplification chains in superconducting qubit platforms. By adding only the minimal amount of noise permitted by the laws of quantum mechanics, these amplifiers have proven invaluable for amplifying weak microwave signals encoding the quantum state of superconducting qubits [4–9]. Other quantum systems, including spin-qubit implementations [10–14], and novel types of hybrid semiconductor-superconductor qubits [15–18], as well as condensed-matter experiments [19,20] are generally done or operated under magnetic fields and therefore require magnetic-field-compatible parametric amplifiers. An additionally desired feature is minimal crosstalk to sensitive structures in the vicinity of the amplifier, such as flux-tunable qubits. However, conventional superconducting parametric amplifiers with flux-biased [21–25] or current-biased [26] control are impractical to operate near flux-sensitive elements. Surpassing these limitations necessitates the development of novel types of parametric amplifiers combining magnetic field compatibility with a new source of tunability.

Recent technological advances in the integration of exotic heterostructures into superconducting circuits, such as hybrid superconducting-semiconducting nanostructures [15,27–32], graphene Josephson junctions [19,33,34], or carbon-nanotube junctions [35], have enabled the realization of electrostatic control of supercurrents in superconducting circuits. This additional method of tunability has already opened up new avenues to build novel types of parametric amplifiers from graphene [36,37] and proximitized semiconductors [38], further advancing the development of densely packed superconducting electronics due to minimal crosstalk. Concurrently, magnetic field compatibility of parametric amplifiers has been achieved through the use of superconducting thin films acting as kinetic inductance material [39–41].

*l.j.splitthoff@gmail.com

In this work, we leverage the continuous superconducting aluminum thin film on an InAs nanowire, which can be seen as a chain of infinitesimally short, gate-tunable Josephson junctions to experimentally demonstrate a magnetic-field-compatible, gate-tunable kinetic inductance parametric amplifier composed of an InAs/Al nanowire shunting a Nb-Ti-N coplanar-waveguide resonator [30]. Notably, the parametric amplifier presented in this work features a gate-tunable amplification window, and magnetic field compatibility resulting from the superconducting thin film and the Josephson-junction-free design. Moreover, the amplifier exhibits a substantial saturation power and increased resilience against electrostatic discharge compared with Josephson-junction-based implementations, owing to the continuous superconducting film.

II. EXPERIMENTAL SETUP

In our realization, we use a quarter-wave coplanar-waveguide resonator that is capacitively coupled to a launch pad at one end and shorted to ground via a proximitized InAs/Al nanowire; see Fig. 1(a). The frequency of the resonator is controlled with a dc voltage applied to the gate line [see the purple structure in Fig. 1(a)]. To minimize losses of the coplanar waveguide, we implement a fifth-order Chebyshev *LC* filter that suppresses coupling to the gate line by at least 50 dB within a frequency range of 4–8 GHz; see Appendix A for additional details on the device design and the *LC* filter. For electrostatic control, we follow Ref. [30] and place the nanowire of length $l = 4.5$ μm on an electrostatic voltage gate that extends for 3.5 μm below the nanowire segment; see Fig. 1(b). The nanowire section is directly connected to the central conductor of the resonator and to ground via thick Nb-Ti-N patches. The schematic representation of the proximitized nanowire in Fig. 1(c) highlights the continuous Al shell covering two facets of the InAs nanowire [42]. We maximize the magnetic field compatibility by aligning the magnetic field parallel ($B_\parallel$) with the nanowire.

The nanowire-shunted resonator is expected to exhibit a nonlinear Kerr-type behavior when driven near resonance, where the resonance frequency shifts linearly with respect to the number of microwave photons occupying the resonator mode; see also Appendix B. As a result, it is natural to use the nonlinear resonator as a parametric amplifier in the nondegenerate mode, which preserves the phase of the input signal. This mode of operation takes advantage of the four-wave-mixing process occurring within a Kerr oscillator. This process involves the interaction of two pump photons, at frequency f_p, and one signal photon, at frequency f_s, leading to the conversion of a pair of pump photons into an idler photon at f_i and an additional signal photon, which therefore leads to amplification of the signal tone [as illustrated in Fig. 1(d)]. We integrate a circulator at the input to the device to ensure that the signal and pump photons pass through the parametric amplifier, while also maintaining the desired directionality from the input to the output spectrum. Overall, this experimental configuration enables efficient phase-preserving amplification of the input signal; see also Appendix C for a detailed description of the experimental setup.

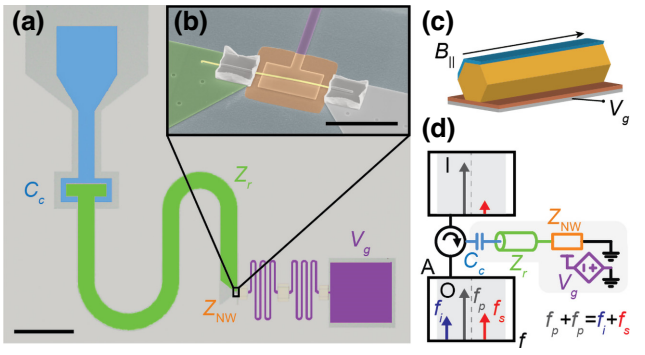

FIG. 1. Device and equivalent circuit. (a) False-color optical-microscope image of a gate-tunable parametric amplifier comprising a quarter-wave coplanar-waveguide resonator (green) that is capacitively coupled to the reflection port (blue) and shorted to ground (light gray) via a proximitized nanowire (yellow). The gate line with a fifth-order Chebyshev *LC* filter (purple) suppresses the crosstalk between the resonator and the gate line. (scale bar 250 μm). (b) Electron micrograph of the nanowire segment. The nanowire is connected with thick Nb-Ti-N patches to the resonator and ground. (scale bar 5 μm). (c) Schematic representation of the InAs nanowire (yellow) that is proximitized with a continuous Al shell (blue) on two facets and positioned on a voltage gate (gray) with a dielectric (orange). (d) Equivalent circuit of the parametric amplifier and representation of the four-wave-mixing operation showing the signal amplitude A as a function of frequency f. At the input (I), a pump tone (gray) with frequency f_p and a signal (red) with a frequency f_s enter the nonlinear resonator. At the output (O), the signal is amplified and there is an additional idler tone with frequency f_i. The dashed line indicates the central frequency of the undriven resonator and the gray box is the amplifier bandwidth.

III. EXPERIMENTAL RESULTS

A. Gate-tunable nonlinear resonator

To characterize the parametric amplifier, we start by measuring the complex transmission parameter S_{21} between the input port and the output port to extract the resonance frequency of the resonator as well as the internal and coupling quality factors. These quantities are extracted from a fit to a complex Lorentzian as expected for linear, reflection-type resonators [43,44]. The resonance frequency is tunable with the gate voltage and we observe a monotonic increase in resonance frequency for voltages within the range from −3 to 7 V; see Fig. 2(a). The shift of about 15 MHz arises from a change in the kinetic inductance associated with the proximitized nanowire, as shown

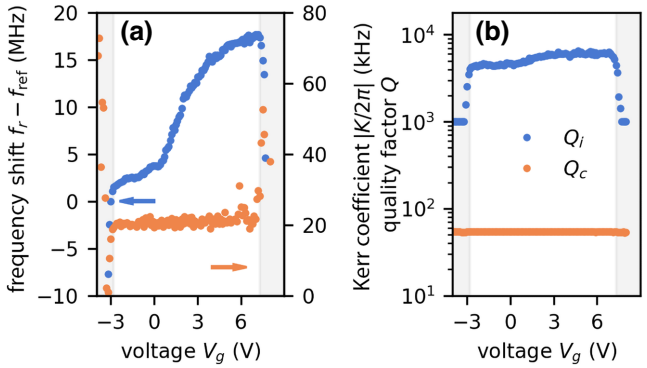

FIG. 2. Gate-tunable nonlinear resonator. (a) Frequency shift (blue, left axis) relative to the reference frequency f_{ref} measured at $V_g = -3$ V and Kerr coefficient K (orange, right axis) as function of gate voltage V_g. (b) Internal quality factor Q_i (blue) and coupling quality factor Q_c (orange) as a function of gate voltage V_g. The gray shaded areas indicate regions of suppressed resonator quality for gate voltages below −3 V and above 7 V.

in Ref. [30]. The nearby voltage gate controls the charge carrier density in the nanowire and hence the normal-state conductivity, which dominates the high-frequency response. At the same time, the superconducting gap closes only partially with increasing gate voltage. To characterize the nonlinearity of the resonator, we increase the power of the spectroscopy tone and we extract a Kerr coefficient K as the linear slope of the resonator frequency as a function of inferred photon number inside the resonator. We find $K \approx 20$ kHz for all gate voltages, which lies between typical values reported for parametric amplifiers based on a single junction [36] and for kinetic-inductance-based amplifiers [39]. The flat response versus gate voltage facilitates a robust tune-up of the device in contrast to previous voltage-tunable junction-based systems, where the Kerr coefficient strongly depends on the gate voltage [36–38]. The internal quality factor increases slightly over the accessible gate-voltage range starting at $Q_i \sim 4000$, whereas the coupling quality factor stays nearly constant at $Q_c \sim 50$. The increase in Q_i could be attributed to the finite gap at all gate voltages and the addition of further conduction channels with more-positive gate voltage, although a detailed study of the internal-loss mechanism is beyond what can be extracted from simple spectroscopy measurements. In addition, we observe a small, although negligible for the applications considered here, reduction of Q_i due to nonlinear losses (see Fig. 7). Outside the −3 to 7 V voltage range, indicated by gray boxes in Fig. 2, the resonator coherence is suppressed by gate leakage. The n-doped Si substrate forms a Schottky junction below about −3 V voltage bias, leading to the injection of quasiparticles. Above 7 V, we observe the breakdown of the SiN gate dielectric. These range limitations could be mitigated in the future by alternative material choices for the dielectric medium.

B. Amplifier characteristics

Next, we demonstrate that the nonlinear resonator can be operated as a parametric amplifier. We apply a strong pump tone slightly detuned from the bare resonance frequency and we measure the signal gain for signal frequencies in the vicinity of the pump; see Fig. 3(a). Notably, we find that by changing the gate voltage, the points of maximal gain shift to different frequencies, exemplified for five different gate voltages in Fig. 3(a). Specifically, we find that the amplifier exhibits more than 20-dB gain in all tested configurations, yielding a gate-tunable amplification window of more than 15 MHz. In nominally identical devices but different experimental realizations, we have observed accessible frequency tuning ranges of more than 70 MHz. It is important to note that the gate dependence of the parametric amplifier's working point exhibits a nonmonotonic behavior, which is in contrast to the monotonic frequency response observed in Fig. 2(a), resulting

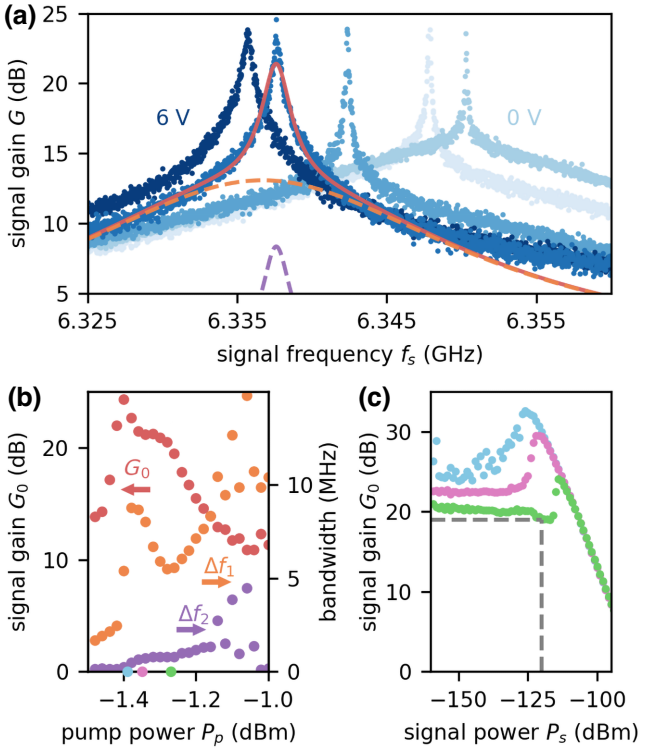

FIG. 3. Amplifier characteristics. (a) Signal gain versus signal frequency for different gate-voltage settings (6, 4, 2, 0, and −2 V] from dark to light shades. The solid red curve shows the best fit of a double Lorentzian to the gain curve. The dashed purple and orange curves show the individual single-Lorentzian curves composing the fits. (b) Signal gain, G_0, and bandwidths of the two Lorentzian curves, Δf_1 and Δf_2, as a function of pump power at the signal generator, P_p, at room temperature. (c) Signal gain as a function of referred signal power at the PA input, P_s, for three different pump powers indicated on the x axis of (b) with color-matching markers.

from an interplay between the linear and nonlinear inductances. However, while the gate dependence of the optimal working point cannot be *a priori* predicted, we find only a weak hysteresis versus gate voltage, as reported in earlier work [30], which allows a robust and efficient tune-up as well as stable operation over days of the parametric amplifier.

We fit the signal-gain curve with a double-Lorentzian model that captures both the up-to-15-dB broadband amplification window (orange) and the narrowband mode (purple) centered at the pump frequency; see Fig. 3(a). This double-Lorentzian behavior may arise from the presence of a parasitic mode, most likely a box mode stemming from the sample enclosure. Note that the fit underestimates the maximal gain observed in the gain curve. Despite this complex mode structure, we extract the maximal signal gain G_0 of the fitted response versus pump power P_p and find a stable working range of 0.1 dB with more than 20-dB gain, see Fig. 3(b), which exemplifies the trend at a gate setting of +4 V. The bandwidths of the two respective modes Δf_1 and Δf_2 evolve nonmonotonically as a function of power. While Δf_1 increases for pump powers above -1.25 dB, Δf_2 stays nearly constant. The trend of the gain curve (red) and the contribution to the bandwidth of the broad mode (orange) can be explained by considering a single-mode-Kerr-resonator model for a fixed pump frequency ω_p and a variable pump strength ξ. Since the optimal pump frequency depends on the pump power, the system deviates from the optimal pump condition and the low-order approximation yielding a constant gain-bandwidth product breaks down. Instead, we expect a minimal bandwidth (orange curve) at the point of maximal gain (red), which is in agreement with the data shown in Fig. 3(b) around -1.25 dBm. For larger pump powers, the bandwidth increases and the gain decreases as expected but because of the second mode we do not reach the coupling-limited gain-bandwidth product. This simple description does not capture the regime of pump powers below -1.4 dBm, when the distinction of the two modes becomes unreliable due to the small gain and small bandwidth. Consequently, the gain-bandwidth product of neither mode reaches the bandwidth limit of 128 MHz set by the coupling quality factor of the resonator, as would be expected for an ideal single-mode Kerr resonator close to the optimal pump condition. To characterize the dynamic range of amplification, we record the maximal signal gain G_0, directly extracted from the data, versus signal power, as shown in Fig. 3(c) for three different pump powers as indicated with colored dots in Fig. 3(b). With increasing signal power, the signal gain overall reduces due to a deviation from the stiff pumping condition [1,2]. For a weak signal gain of 20 dB, we observe a 1-dB compression point of -120 dBm, which is on par with the saturation powers reported in work on other capacitively coupled superconducting-quantum-interference-device (SQUID), SQUID-array, and single-junction and gate-tunable-junction implementations [36–38] (see also Table I) and should allow frequency-multiplexed qubit readout given a sufficiently large amplification bandwidth. The sharp rise in the signal gain before its overall decrease, sometimes referred to as a "shark fin," results from an interplay between the input signal and the internal dynamics of the parametric amplifier due to higher-order nonlinear terms at negative pump detuning. This gain-rise phenomenon has been observed experimentally [25,45] and has been described theoretically [46–48].

C. Noise performance

While large gain is desirable for parametric amplifiers, it should come without the cost of additional added noise beyond the quantum limit, so as not degrade the amplifier performance. We generally quantify the quality of a signal by considering the SNR. Specifically, we compare the power level of the signal to the power level when the signal is turned off or, more practically, the power level slightly detuned from the signal. For an amplifier, we can define the SNR improvement as the difference in the SNR between the ON state and the OFF state of the amplifier $\Delta\mathrm{SNR} = \mathrm{SNR}_{\mathrm{on}} - \mathrm{SNR}_{\mathrm{off}}$, which serves as a good measure for its noise characteristic. For the parametric amplifier that we study here, we find that the SNR improvement depends strongly on the pump power and pump frequency as shown in Fig. 4(a), measured at a gate voltage of +4 V and at a signal-pump detuning Δ of 0.5 MHz. The SNR improvement reaches a maximum of about 7 dB, which is about 2 dB lower than the theoretical maximum set by the difference between the noise temperature of the high-mobility-electron transistor (HEMT) and the quantum limit [49]; see Fig. 4(b). It is worth noting that the maximal SNR improvement versus pump power presented in Fig. 4(c) does not coincide with the maximum in the gain curve, but shows a peak at about 15-dB signal gain. Note that we slightly compress an amplifier at room temperature when maximal gain is being approached, which might have led to the slight shift between the point of maximal gain with respect to the point of maximal SNR improvement in Fig. 4(c). Also note that the working point of the parametric amplifier has shifted by about 10 MHz compared with the data shown in Fig. 2(a) after many gate scans, which might have led to a different charge configuration in the nanowire [50] and hence to a slightly different working point. In Fig. 4(b), we compare the spectrum obtained for a single pump tone between the driven state and the undriven state of the parametric amplifier. In the undriven case, the noise is limited by the HEMT amplifier at the 4-K stage of the cryostat. The referred power, and hence the effective noise temperature, is estimated on the basis of a line calibration supported by an estimate based on the dispersive shift of an adjacent on-chip transmon qubit connected to the input port (see Appendix D).

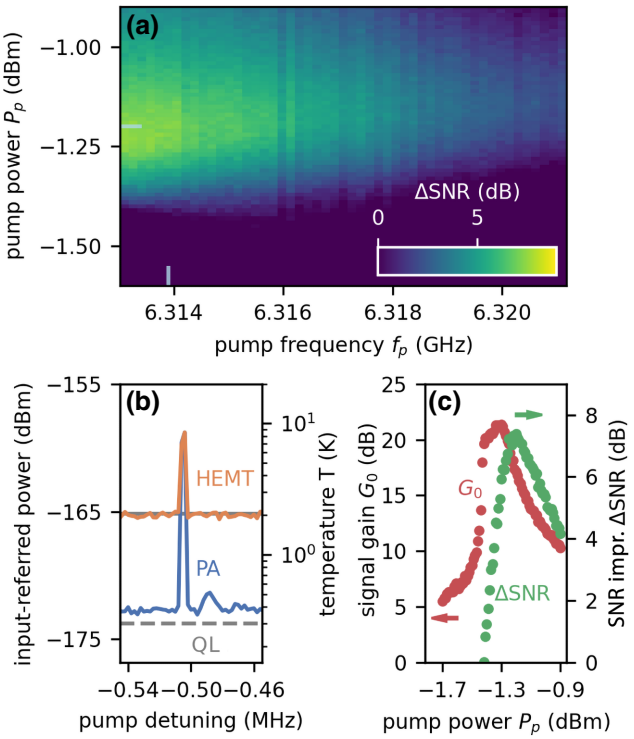

FIG. 4. SNR improvement. (a) Change in the signal-to-noise ratio as a function of pump power, P_p, and pump frequency, f_p, for a fixed detuning between the signal frequency and the pump frequency of 0.5 MHz. Light-blue lines indicate the working point used for the trace shown in (b). (b) Input-referred power spectrum with signal tone at 6.3134 GHz and pump tone at 6.3139 GHz in the undriven (orange) and driven (blue) cases. The dashed lines indicate the quantum limit (QL) and the specified noise temperature of the HEMT for a resolution bandwidth of 1 kHz. For comparison, the equivalent temperature is provided on the right axis. (c) Signal gain (red, left axis) and SNR improvement (green, right axis) versus pump power for $f_p =$ 6.3139 GHz.

In the undriven case, we observe the signal tone at 6.3134 GHz and the pump tone leaking through the output of the signal generator, while the noise floor is set by the noise temperature of the HEMT, which is close to the manufacturer-specified value of 2.2 K indicated as a horizontal gray line. In the driven case, the signal amplitude increases together with the appearance of an idler tone of about the same magnitude, while the noise floor drops below the noise floor of the HEMT, showcasing the usefulness of the parametric amplifier presented here. While the increase in SNR is noteworthy, we also observe that the performance is not fully quantum limited as we do not reach the quantum limit of 303 mK, indicated by a dashed gray line in Fig. 4(b). The inability to reach the quantum limit signals the presence of an additional loss channel in the system, which is consistent with the observations of an additional mode in Fig. 3.

D. Magnetic field compatibility

The continuous superconducting thin film renders amplification at high magnetic field strength possible, since the superconducting gap is not locally suppressed inside a Josephson junction, potentially leading to interference effects. In particular, we are interested in magnetic fields of up to a few hundred milliteslas as used for a variety of spin-based devices [13] and hybrid superconductor-semiconductor devices [16,18]. When the magnetic field, $B_\parallel$, is aligned with the nanowire direction, the compatibility with the field should be maximal, and we observe up to 20-dB gain at fields up to 0.5 T; see Fig. 5. Moreover, at 0.5 T, we see maximal gain at a 170-MHz-lower signal frequency compared with the zero-field setting. The overall shift of the amplification window towards lower frequencies along with the increase in the Kerr coefficients follows from the continuous suppression of the superconducting gap with magnetic field [30]. The nonmonotonicity of the frequency shift and the lower maximal gain can be attributed to the nucleation of vortices in the heterostructure of finite thickness and to small field misalignments [51], a scenario that is most-likely unavoidable in real applications of this amplifier. The distortion of the gain curves in Fig. 5 arises most likely from a Fano interference with a broad box mode [52]. We did not explore the magnetic field dependence of the parametric amplifier beyond 0.5 T, nor did we characterize the noise performance at elevated magnetic fields due to technical limitations imposed by the dilution refrigerator that prevented us from maintaining an elevated field while keeping the base temperature cold. However, we do not expect a significant change in the noise performance as the resonator loss rate γ remains smaller than the coupling strength κ. While an increase in the resonator loss rate γ is unavoidable, previous work on similar hybrid systems allowed the realization of a transmon qubit operated at 1 T [53], which shows that the fabrication of coherent devices at elevated

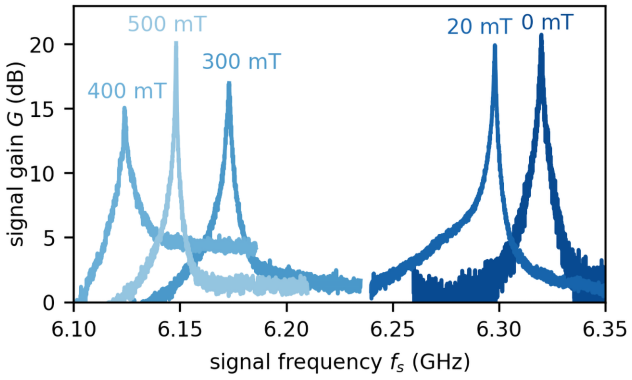

FIG. 5. Magnetic field compatibility. Signal gain versus signal frequency for the parallel-magnetic-field strengths of 0, 20, 300, 400, and 500 mT.

magnetic field is possible. Note that this dataset was taken in a consequent cooldown, which again led to a different charge configuration in the nanowire and hence a different working point.

IV. CONCLUSION

We experimentally demonstrated a prototype of a gate-tunable kinetic inductance parametric amplifier. This system features a gate-tunable amplification window of up to 15 MHz due to the hybrid superconducting-semiconducting nanostructure, magnetic field compatibility up to at least 500 mT due to the superconducting thin film, a sizable saturation power of −120 dBm, and minimal electrostatic discharge sensitivity due to the continuous superconducting film. The tuning range of the amplification window reported here should be sufficient to render frequency matching with other superconducting resonators made from low-kinetic-inductance film and hence low fabrication-induced frequency variability [54] possible. Furthermore, we expect that the local gate-voltage control, as demonstrated here, will exhibit minimal crosstalk to other voltage-controlled elements due to the absence of finite and long-range supercurrents induced by the dc control. Thus, this ability to tune the nonlinear resonator might render large-scale implementations of voltage-controlled superconducting electronics with dense packing possible.

While this demonstration of a gate-tunable kinetic inductance parametric amplifier achieves the main objectives of magnetic field compatibility, gate tunability, and a useful saturation power, further improvements must be made without additionally compromising any of these features. Therefore, further work should be devoted to the improvement of the dielectric environment to widen the tuning range without being limited by current leakage at higher voltages. Moreover, the optimization of the inductance ratio of the proximitized nanowire and the resonator is required to further increase the saturation power of the amplifier. In this work, we study only four-wave-mixing operations, but three-wave mixing should be accessible by driving the nonlinear resonator via an oscillating voltage gate connected to the proximitized nanowire or alternatively a dc bias through the nonlinear inductor. We expect that three-wave mixing will allows large spectral separation of the pump tone and the signal tone, alleviating frequency crowding in the amplification window and saturation of higher amplification stages.

The raw data and the analysis script underlying all figures in this paper are available online [55].

ACKNOWLEDGMENTS

We thank Peter Krogstrup for the nanowire growth. We also thank Alessandro Miano, Patrick Winkel, Nicolas Zapata González, and Ioan Pop for valuable discussions. This research was cofunded by the Top consortia for Knowledge and Innovation (TKI) from the Dutch Ministry of Economic Affairs and the Microsoft Quantum initiative. C.K.A. acknowledges financial support from the Dutch Research Council (NWO).

L.J.S. and C.K.A. conceived the experiment. L.J.S. fabricated the devices, and acquired and analyzed the data with help from J.J.W., M.P.-V., and A.B. Y.L. provided the proximitized nanowires. L.J.S. and C.K.A. wrote the manuscript with input from all other coauthors. C.K.A. supervised the project.

APPENDIX A: DESIGN AND FABRICATION

1. Design

We design the circuitry using a customized design framework [56]. The loaded quarter-wave resonator is designed to have a total capacitance C_0 of 511 fF, a total inductance L_0 of 1.07 nH for the unloaded transmission-line resonator, a capacitance to the input port of C_c of 55 fF, and an inductance for the proximitized nanowire L_{NW} of 0.79 nH. We note that if the nanowire segment were a single Josephson junction, we would expect a critical current $I_c = \Phi_0/2\pi L_{\mathrm{NW}}$ of approximately 0.42 μA for this inductance. Instead, in dc experiments on nanowires from the same batch, we measure a critical current of around 3–17 μA, which quantitatively supports the description of the nanowire as a kinetic inductance element. The nanowire inductance fraction α in in this configuration is $L_{\mathrm{NW}}/(L_{\mathrm{NW}} + L_0) = 0.42$. The quarter-wave-transmission-line design frequency separates best the fundamental mode from higher harmonics simulated to be above 19.2 GHz. To suppress crosstalk between the amplifier mode and the voltage gate, we add a fifth-order Chebyshev low-pass filter in between. The filter is composed of three parallel-plate capacitors and two meandering inductors as shown in Fig. 1(a). As expected for a low-pass filter, we

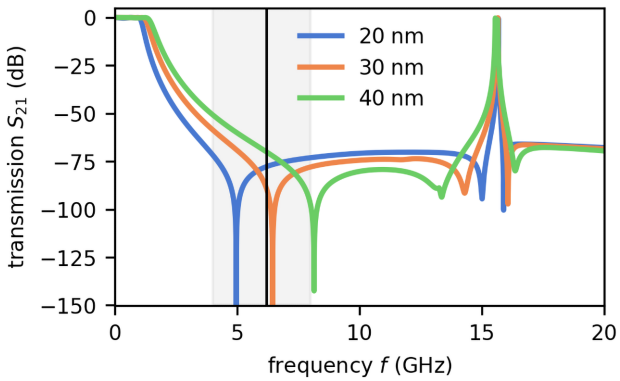

FIG. 6. Filter response. Simulated transmission parameter S_{21} versus frequency of a fifth-order Chebyshev filter for three different dielectric layer thicknesses. The gray box indicates the 4–8-GHz range. The vertical black line indicates the resonance frequency of the undriven amplifier.

find that the filter suppresses high-frequency transmission; see Fig. 6, which shows the low-pass-filter response from finite-element simulations for three different thicknesses of the dielectric material SiN separating the two superconducting plates. The filter therefore suppresses the coupling between the amplifier and the gate by more than 50 dB in the 4–8-GHz range (gray box) also in the case of small fabrication imperfections potentially resulting in the SiN-film thickness. The filter structure also exhibits self-resonances due to its finite length at around 15.5 GHz. In microwave simulations, we do not find any additional or common mode due to the filter structure around the resonance frequency of the undriven amplifier that could explain the appearance of an additional mode in the driven case.

2. Fabrication

We fabricate the resonator circuit and the gate lines from a 40-nm-thick sputtered Nb-Ti-N film (kinetic inductance 4 pH $\square^{-1}$) on high resistivity *n*-doped Si. We pattern the Nb-Ti-N film using electron-beam lithography and SF_6-O_2-based reactive-ion etching. Thirty-nanometer-thick plasma-enhanced-chemical-vapor-deposition SiN defined by a buffered oxide etch serves as the bottom-gate dielectric. We transfer the two-facet InAs/Al nanowire on top of the SiN bottom gate using a nanomanipulator. The InAs nanowires are grown by vapor-liquid-solid growth with a diameter of 110(5) nm and nominal thickness of the Al of 6 nm [42]. We electrically contact the nanowires to the circuit via lift-off-defined 150-nm-thick sputtered Nb-Ti-N leads after prior Ar milling to minimize the contact resistance.

3. Reproducibility

We have prepared 13 samples with four amplifiers each. We have measured seven samples with in total 12 parametric amplifiers in 12 cooldowns, of which six amplifiers exhibit more than 20-dB gain. The remaining devices are discarded because of fabrication imperfections or excluded because of high room-temperature resistances of the nanowire segment due to high nanowire-to-Nb-Ti-N contact resistance.

APPENDIX B: KERR COEFFICIENT

The parametric amplifier is a nonlinear resonator where the nonlinearity, as explained in the main text, manifests itself as a frequency shift proportional to the number of photons in the resonators. We extract this proportionality constant, the Kerr coefficient K, from a measurement of the frequency shift versus intraresonator photon number; see Fig. 7, which shows this measurement for different gate voltages. The frequency shifts are displayed here with respect to the resonator frequency measured at the weakest signal power $f_r, 0$. We observe a similar slope for

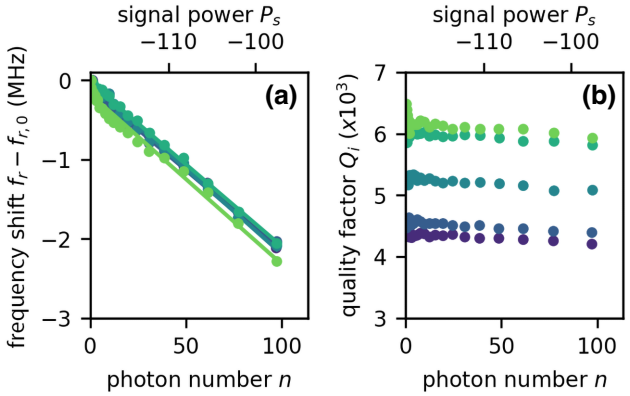

FIG. 7. Nonlinear resonator. (a) Frequency shift and (b) internal quality factor for five different gate voltages between −2.5 and 5.5 V versus intracavity photon number.

all gate voltage between −2.5 and 5.5 V, which results in a Kerr coefficient of about 20 kHz. As shown in Fig. 7, the internal quality factor increases with gate voltage from $Q_{i,-2.5\ \mathrm{V}} = 4363$ to $Q_{i,5.5\ \mathrm{V}} = 6483$, and for all gate voltages, we see a weak dependence of Q_i on the intraresonator photon number.

APPENDIX C: MEASUREMENT SETUP

The 6×6 mm^2 chip hosting the parametric amplifier, and also a readout resonator and transmon qubit (see Appendix D), is glued with GE varnish onto a gold-plated copper mount and electrically connected to a printed circuit board with use of Al wire bonds.

The room-temperature control and readout electronics (red box in Fig. 8) control the sample under test. A signal generator and a vector network analyzer (VNA) are connected to the drive line for the parametric amplifier. Amplitude-modulated waveforms provided by the two other signal generators and two baseband arbitrary-waveform generators drive the transmon qubit and the readout resonator. The output signal is split into a signal path to the vector network analyzer and towards the amplitude-demodulation unit. The microwave components installed in the dilution refrigerator (blue areas in Fig. 8) include two strongly attenuated and low-pass-filtered input lines and one output line, and the sample hosting the readout resonator, the transmon qubit, and the parametric amplifier. The output line is amplified with use of one HEMT operating at cryogenic temperatures (4 K) and one HEMT operating at room temperature as well as the parametric amplifier under test.

The estimation of the line attenuation and amplification between room-temperature electronics and the parametric amplifier is based on a combination of transmission measurements at low temperature and room temperature and is summarized in Fig. 9. The probe line between the VNA and the parametric amplifier has −99-dB attenuation

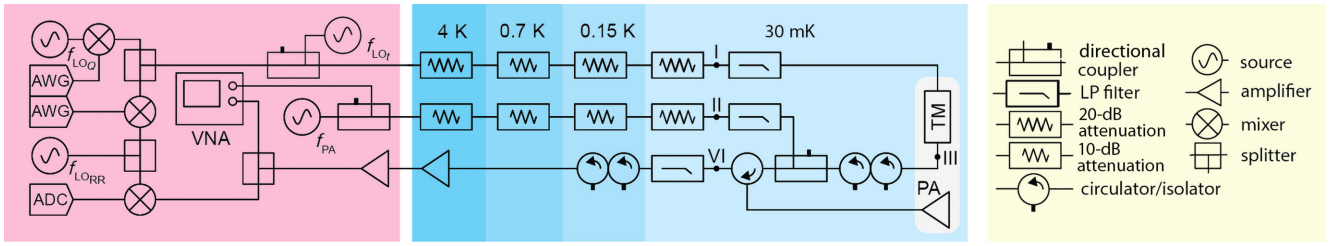

FIG. 8. Experimental setup. Left: Room-temperature control and readout electronics. A signal generator, f_{PA}, and a VNA are combined with a directional coupler and connected to the drive line of the parametric amplifier. Two arbitrary-waveform generators (AWGs) provide modulated waveforms that are up-converted to microwave frequencies with the local oscillators set by two signal generators, f_{LO_Q} and $f_{\mathrm{LO}_{\mathrm{RR}}}$, for the transmon-qubit drive and the readout. The output signal is split into a signal path to the vector network analyzer and towards the analog-to-digital converter (ADC). Middle: Microwave components installed in the dilution refrigerator, including two input lines and one output line. The sample (gray) hosts the readout resonator, the transmon qubit, and the parametric amplifier. Two strongly attenuated and low-pass-filtered input lines serve as a readout resonator and transmon-qubit drive line and as a parametric amplifier drive line. The output line is amplified with use of one cryogenic HEMT and one room-temperature HEMT.

at 6.4 GHz, which is composed of 50-dB cold attenuation between the VNA output and the PA input, 40 dB from the two directional couplers, 3.3-dB attenuation from the Eccosorb filters at 6.4 GHz, 3.2-dB cable and connector loss at room temperature, and the insertion loss of the low-pass filter, circulator, and copper cables connecting to the PA of about 2.5 dB; see the blue line in Fig. 9(a). The connection between the PA drive-signal generator and the parametric amplifier has 20 dB less attenuation due to the through connection through the first directional coupler at room temperature. The attenuation between the local oscillator test-signal generator, which generates the test tone for the SNR-improvement measurement, and the input to the transmon readout resonator is -100 dB. Figure 9(b) shows the attenuation of the interconnections before and after the parametric amplifier, in particular the connection from the transmon-readout-resonator output (III) to the parametric amplifier input with -2.5-dB attenuation and the connection between the PA output and the HEMT input (IV) with -1.3-dB attenuation. Figure 9(c) shows the net amplification of the readout chain for two different tested configurations. The data presented in this paper are based on the "PA $\rightarrow$ VNA*" configuration with 70.7-dB gain provided by the cryogenic HEMT (Low Noise Factory LNF-LNC4_8C serial number 844H, $P_{1\ \mathrm{dB,out,cryo}} = -8$ dBm) and the Low Noise Factory room-temperature HEMT (LNF-LNR4_8F_ART, $P_{1\ \mathrm{dB,out,room\ temperature}} = 0$ dBm), which we test componentwise at room temperature. Finally, we can compare the componentwise characterization for the input lines [Fig. 9(a)] and the output line [Fig. 9(c)] at room temperature with the transmission measurement through the entire setup in the cold state, presented in Fig. 9(d). The sum of the individual input-line and output-line characterizations agrees up to 4 dB with the total transmission measurement from the VNA output port to the VNA input port as shown in the wiring diagram in Fig. 8. This discrepancy might arise from multiple reconnections between the components and a different thermal state of the components in the respective measurements.

This line calibration suggests that the typically used pump power level P_p at the PA of -1.2 dBm $-$ 78.9 dB $=$ -80.1 dBm does not compress the cryogenic HEMT with input saturation power $P_{1\ \mathrm{dB,in,cryo}} \approx -48$ dBm. However, the pump power level after the cryogenic amplifier is about -40 dBm, which is on the level of the 1-dB input compression power $P_{1\ \mathrm{dB,in,room\ temparature}}$ of the room-temperature HEMT of approximately -42 dBm. Consequently, the pump tone together with the amplified signal tone may saturate the room-temperature amplifier in this configuration of the measurement setup, which may distort the gain curves and also cause the shift between the point of maximal gain and the point of maximal SNR improvement, observed in Fig. 4(c). To mitigate the saturation of the room-temperature amplifier, we consider an alternative configuration of the readout chain including a 20-dB attenuator before an alternative room-temperature amplifier with lower gain, but also lower 1-dB compression point. The net amplification of this readout chain is shown as a blue curve in Fig. 9(c). While the gain curves remain the same, we notice that the readout chain is not limited by the HEMT noise temperature anymore but rather is limited by the noise temperature of the spectrum analyzer, which would have complicated the interpretation of the noise characterization considerably.

APPENDIX D: CAVITY-REFERRED POWER ESTIMATED WITH USE OF A TRANSMON QUBIT COUPLED TO A READOUT RESONATOR

To further characterize the noise performance of the parametric amplifier and to showcase its usefulness in terms of co-operation with other quantum devices, we integrate two transmon qubits, which are dispersively coupled

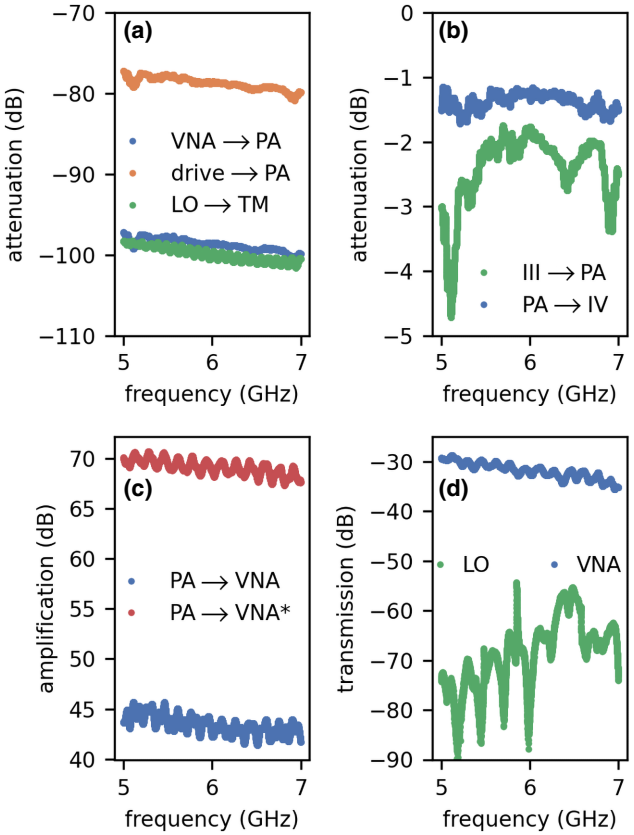

FIG. 9. Transmission calibration of measurement chain and individual components measured with a VNA. (a) Input-line transmission at room temperature from the VNA to the PA input (blue), from the PA drive-signal generator to the PA input (orange), and from the test tone-signal generator to the transmon-readout-resonator (TM) input (green). (b) Interconnection transmission at room temperature from the TM output (III in Fig. 8) to the PA input and from the PA output to the HEMT input (IV in Fig. 8). (c) Net amplification of the readout chain between the PA output and the VNA input for two different configurations. (d) Transmission measurement in the cold state with the PA OFF from the VNA output port to the VNA input port (blue) and from the local oscillator (LO) signal generator generating the test tone to the VNA input (green).

to a common readout resonator on the same device chip as the parametric amplifier. Figure 10(a) shows a false-color optical image of the transmission-line readout resonator that is weakly coupled (C_{C_1} small) to the input port and strongly coupled (C_{C_2} large) to the output port. Two single-island transmon qubits [57] are capacitively coupled close to the current nodes of the resonator; see Fig. 10(b) for the equivalent-circuit diagram. The Josephson junctions of the two transmon qubits are formed by electrostatically controlled proximitized nanowires with an etched segment as displayed in the schematic representation in Fig. 10(c). The gate voltage controls the critical current of the Josephson junction, and hence the Josephson energy

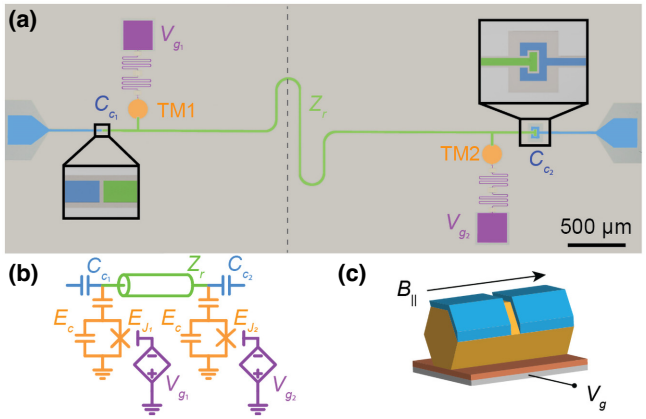

FIG. 10. Transmon qubit and readout resonator. (a) False-color optical microscope image of a readout resonator in transmission-line configuration (green) that is capacitively connected to a weakly coupled input port (blue, left) and a strongly coupled output port (blue, right). Two single-island transmon qubits (orange) labelled TM1 and TM2 are capacitively coupled around the current nodes of the readout resonator. The nanowire Josephson junctions of the transmon qubits are electrostatically controlled via low-pass-filtered voltage gates (purple). The optical image has been cropped at the dashed gray line for better visibility, which reduces the displayed length of the resonator. (b) Equivalent-circuit diagram of the device shown in (a). (c) Schematic representation of the nanowire Josephson junction formed by an InAs nanowire that is partially proximitized with an Al shell on two facets and positioned on a voltage gate.

E_J, but also a global magnetic field affects the Josephson energy. This tuning knob allows us to tune the transmon frequency f_q *in situ* as $hf_q(V_g) \approx \sqrt{8E_cE_J(V_g)} - E_c$ under the assumption of many low-transparency channels in the

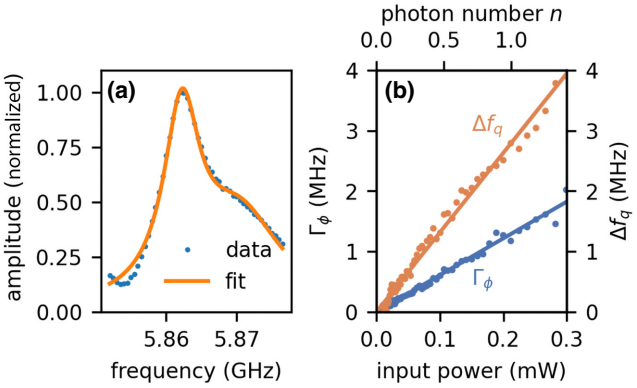

FIG. 11. Estimation of intracavity photon number. (a) Transmission spectrum of the readout resonator with a double-Lorentzian fit. (b) Measurement-induced dephasing (blue, left axis) and frequency shift (orange, right axis) as a function of input power of a readout tone with frequency f_{LO_t} applied during a Ramsey experiment. The data are shown with a linear fit to extract the slope. The equivalent intracavity photon number is indicated on the top axis.

nanowire junction [58]. Here E_c is the charging energy of the transmon island.

To estimate the cavity-referred power P_{out}, we independently measure the dispersive shift χ and the cavity coupling rate κ. We obtain χ from a variable-strength Ramsey experiment [59,60], which allows us to extract the measurement-induced dephasing rate $\Gamma_\phi = 8\chi^2 n/\kappa$ and the qubit frequency shift $\Delta f_q = 2\chi n$ as a function of a weak test tone at the readout-resonator frequency applied with use of a signal generator at frequency f_{LO_t} during the idling time of the qubit in the equal superposition state; see Fig. 11(b). From a linear fit to the dephasing rate Γ_ϕ versus input power at the signal-generator output P_{SG}, we obtain the slope $\partial_P \Gamma_\phi$. Similarly, a linear fit to the frequency shift Δf_q yields $\partial_P \Delta f_q$. Their ratio yields the dispersive shift χ expressed in the following equation:

$$\chi = \frac{\kappa}{4} \frac{\partial_P \Gamma_\phi}{\partial_P \Delta f_q}. \tag{D1}$$

From a linear fit to the frequency shift $\Delta f_q = 2\chi c P_{\text{SG}}$, we obtain the conversion factor c, which allows us to compute the intraresonator photon number n as cP_{SG}. Finally, the cavity-referred power at the resonator output is given by $P_{\text{out}} = \kappa h f_r n$. Because of the directional design of the transmission-line resonator with $C_{C_2} \gg C_{C_1}$ and high internal quality factor $Q_i > Q_c$, we can approximate the coupling rate κ as f_r/Q_{tot}, which is equivalent to the FWHM of the peak in the transmission measurement extracted from the double-Lorentzian fit in Fig. 11(a). At one specific gate set point for transmon qubit 1 ($V_{g_1} = 0.75$ V) and while transmon qubit 2 is frequency detuned with the pinched-off nanowire Josephson junction ($V_{g_2} = -2$ V), we find a dispersive shift χ of 1.33 MHz, a cavity coupling rate κ of 11.34 MHz, and a setup-specific conversion factor c of 5.65 mW^{-1}; see Fig. 11. For this configuration, the other system parameters are the resonator frequency $f_r = 5.862$ GHz, the qubit frequency $f_{q_1} = 4.827$ GHz, and the coherence time

TABLE I. Parameter overview of some resonator parametric amplifiers: coupling, design, wave mixing, highest amplifier frequency (f_r), gain-bandwidth product (GBW), input saturation power for about-20-dB weak signal gain (P_{sat}), nonlinear element [NLE; single SQUIDs, SQUID arrays, asymmetric SQUIDs as superconducting nonlinear asymmetric inductive elements (SNAILs), rf-SQUID arrays, graphene-based Josephson junctions (JJs), InAs 2DEG Josephson junctions, InAs nanowire kinetic inductances (KIs), and kinetic inductances from NbN and Nb-Ti-N], frequency tunability achieved by flux, electrostatic gate (EG), magnetic field (MF), or current, and tested magnetic field compatibility up to the specified in-plane magnetic field. BM, Bragg mirror; C, capacitive; CPW, coplanar waveguide; D, direct; DE, distributed element; I, inductive/galvanic; IM, "fishbone" impedance matching; K, Klopfenstein; LE, lumped element; ST, step transformer.

Study	Year	Coupling	Design	Wave mixing	f_r (GHz)	GBW (MHz)	P_{sat} (dBm)	NLE	Tunability	MF (T)
Castellanos and Lehnert [22]	2007	C	DE	4	7.8	3	···	SQUID array	Flux	···
Castellanos *et al.* [23]	2008	C	DE	4	7	11	···	SQUID array	Flux	···
Yamamoto *et al.* [21]	2008	C	CPW	3	11	63	−140	SQUID	Flux	···
Mutus *et al.* [61]	2013	I	LE	3, 4	7	···	−120	SQUID	Flux	···
Zhong *et al.* [24]	2013	C	CPW	3	5.6	15	−136	SQUID array	Flux	···
Zhou *et al.* [25]	2014	C	LE	3	6.0	60	−123	SQUID array	Flux	···
Mutus *et al.* [62]	2014	K	LE	3	6.6	3900	−110	SQUID	Flux	···
Planat *et al.* [63]	2019	D	DE	4	6.8	300	−117	SQUID array	Flux	···
Sivak *et al.* [47]	2019	C	DE	3	7.2	250	−102	SNAILs	Flux	···
Sivak *et al.* [64]	2020	C, I	DE	3	12	110	−108	SNAILs	Flux	···
Winkel *et al.* [65]	2020	I	DE	4	8.0	150	−118	SQUID arrays	Flux	···
Grebel *et al.* [66]	2021	ST	LE	3, 4	5.3	3000	−116	SQUID	Flux	···
Lu *et al.* [67]	2022	IM	LE	3	6.6	2500	−114	SQUID	Flux	···
White *et al.* [68]	2022	K	LE	3	7	3000	−95	rf-SQUID array	Flux	···
Sarkar *et al.* [37]	2022	D	LE	4	5.3	158	−130	Graphene-based JJ	EG	···
Butseraen *et al.* [36]	2022	C	CPW	4	6.2	33	−123	Graphene-based JJ	EG	···
Ezenkova *et al.* [69]	2022	ST	LE	3	6.4	2100	−100	SNAILs	Flux	···
Parker *et al.* [26]	2022	BM	LE	3	6.4	53	···	Nb-Ti-N KI	Current	···
Qing *et al.* [70]	2023	K	LE	3	7.1	3900	-110	SQUID	Flux	···
Xu *et al.* [40]	2023	C	LE	4	7.5	59	–	NbN KI	MF	0.5
Khalifa and Salfi [39]	2023	C	DE	4	4.6	···	···	Nb-Ti-N KI	MF	2
Phan *et al.* [38]	2023	C	CPW	4	6.0	40	−125	2DEG JJ	EG	15×10^{-3}
This work	2023	C	CPW	4	6.1	30	−120	Nanowire KI	EG	0.5
Vaartjes *et al.* [71]	2023	BM	LE	3	6.2	17	−86	Nb-Ti-N KI	Current	2
Frasca *et al.* [72]	2023	ST	DE	3	5.8	21	−86	NbN KI	Current	6

$T_1 = 1.3$ μs. Consequently, a signal-generator input power P_{in} of −20 dBm corresponds to a cavity output power P_{out} of −138.09 dBm at a frequency f_r of 5.862 GHz. Since the transmon readout resonator is not resonant with the parametric amplifier, the SNR measurements presented in Fig. 4 were performed with a signal tone far detuned from the readout-resonator frequency. Away from the passband of the readout resonator, we find that the transmission through the resonator is suppressed between 20 and 25 dB. Therefore, the effective power level at the input of the parametric amplifier, when driven at a signal frequency of around 6.3 GHz with $P_{in} = -20$ dBm at the signal generator, is expected to be in the range from −158 to −163 dBm, which is consistent with the power level inferred from the line calibration and used in Fig. 4(b). Note that we were not able to accurately estimate the precise transmission at the signal frequency of the parametric amplifier due to an unexplained background signal in the transmission spectrum when measured through the readout resonator. Thus, we base the power-level calibration in the main text solely on the line-calibration data.

APPENDIX E: COMPARISON OF THE GATE-TUNABLE PARAMETRIC AMPLIFIER WITH OTHER IMPLEMENTATIONS

To put this work on gate-tunable and magnetic-field-compatible parametric amplifiers into perspective, we present Table I, which collects many resonator-based-parametric-amplifier parameters from a variety of publications addressing several design objectives, such as a wide bandwidth, large saturation power, gate tunability, and magnetic field compatibility. From Table I, it is evident that our implementation is on par with other capacitively coupled SQUID, SQUID-array, and single-junction implementations in terms of bandwidth and saturation power.

[1] C. Eichler and A. Wallraff, Controlling the dynamic range of a Josephson parametric amplifier, EPJ Quantum Technol. **1**, 2 (2014).

[2] A. Roy and M. Devoret, Introduction to parametric amplification of quantum signals with Josephson circuits, C. R. Phys. **17**, 740 (2016).

[3] J. Aumentado, Superconducting parametric amplifiers: The state of the art in Josephson parametric amplifiers, IEEE Microw. Mag. **21**, 45 (2020).

[4] B. Yurke, L. R. Corruccini, P. G. Kaminsky, L. W. Rupp, A. D. Smith, A. H. Silver, R. W. Simon, and E. A. Whittaker, Observation of parametric amplification and deamplification in a Josephson parametric amplifier, Phys. Rev. A **39**, 2519 (1989).

[5] A. A. Clerk, M. H. Devoret, S. M. Girvin, F. Marquardt, and R. J. Schoelkopf, Introduction to quantum noise, measurement, and amplification, Rev. Mod. Phys. **82**, 1155 (2010).

[6] B. Abdo, F. Schackert, M. Hatridge, C. Rigetti, and M. Devoret, Josephson amplifier for qubit readout, Appl. Phys. Lett. **99**, 162506 (2011).

[7] R. Vijay, D. H. Slichter, and I. Siddiqi, Observation of quantum jumps in a superconducting artificial atom, Phys. Rev. Lett. **106**, 110502 (2011).

[8] P. Krantz, A. Bengtsson, M. Simoen, S. Gustavsson, V. Shumeiko, W. D. Oliver, C. M. Wilson, P. Delsing, and J. Bylander, Single-shot read-out of a superconducting qubit using a Josephson parametric oscillator, Nat. Commun. **7**, 11417 (2016).

[9] T. Walter, P. Kurpiers, S. Gasparinetti, P. Magnard, A. Potočnik, Y. Salathé, M. Pechal, M. Mondal, M. Oppliger, C. Eichler, and A. Wallraff, Rapid high-fidelity single-shot dispersive readout of superconducting qubits, Phys. Rev. Appl. **7**, 054020 (2017).

[10] X. Mi, M. Benito, S. Putz, D. M. Zajac, J. M. Taylor, G. Burkard, and J. R. Petta, A coherent spin–photon interface in silicon, Nature **555**, 599 (2018).

[11] F. Borjans, X. G. Croot, X. Mi, M. J. Gullans, and J. R. Petta, Resonant microwave-mediated interactions between distant electron spins, Nature **577**, 195 (2020).

[12] T. Kobayashi, J. Salfi, C. Chua, J. van der Heijden, M. G. House, D. Culcer, W. D. Hutchison, B. C. Johnson, J. C. McCallum, H. Riemann, N. V. Abrosimov, P. Becker, H.-J. Pohl, M. Y. Simmons, and S. Rogge, Engineering long spin coherence times of spin–orbit qubits in silicon, Nat. Mater. **20**, 38 (2021).

[13] S. G. J. Philips, M. T. Mądzik, S. V. Amitonov, S. L. de Snoo, M. Russ, N. Kalhor, C. Volk, W. I. L. Lawrie, D. Brousse, L. Tryputen, B. P. Wuetz, A. Sammak, M. Veldhorst, G. Scappucci, and L. M. K. Vandersypen, Universal control of a six-qubit quantum processor in silicon, Nature **609**, 919 (2022).

[14] A. R. Mills, C. R. Guinn, M. M. Feldman, A. J. Sigillito, M. J. Gullans, M. T. Rakher, J. Kerckhoff, C. A. C. Jackson, and J. R. Petta, High-fidelity state preparation, quantum control, and readout of an isotopically enriched silicon spin qubit, Phys. Rev. Appl. **18**, 064028 (2022).

[15] G. de Lange, B. van Heck, A. Bruno, D. J. van Woerkom, A. Geresdi, S. R. Plissard, E. P. A. M. Bakkers, A. R. Akhmerov, and L. DiCarlo, Realization of microwave quantum circuits using hybrid superconducting-semiconducting nanowire Josephson elements, Phys. Rev. Lett. **115**, 127002 (2015).

[16] M. Pita-Vidal, A. Bargerbos, R. Žitko, L. J. Splitthoff, L. Grünhaupt, J. J. Wesdorp, Y. Liu, L. P. Kouwenhoven, R. Aguado, B. van Heck, A. Kou, and C. K. Andersen, Direct manipulation of a superconducting spin qubit strongly coupled to a transmon qubit, Nat. Phys. **19**, 1110 (2023).

[17] M. Pita-Vidal, J. J. Wesdorp, L. J. Splitthoff, A. Bargerbos, Y. Liu, L. P. Kouwenhoven, and C. K. Andersen, Strong tunable coupling between two distant superconducting spin qubits, ArXiv:2307.15654 (2023).

[18] T. Dvir, G. Wang, N. van Loo, C.-X. Liu, G. P. Mazur, A. Bordin, S. L. D. ten Haaf, J.-Y. Wang, D. van Driel, F. Zatelli, X. Li, F. K. Malinowski, S. Gazibegovic, G. Badawy, E. P. A. M. Bakkers, M. Wimmer, and L. P. Kouwenhoven, Realization of a minimal Kitaev chain in coupled quantum dots, Nature **614**, 445 (2023).

[19] J. I.-J. Wang, D. Rodan-Legrain, L. Bretheau, D. L. Campbell, B. Kannan, D. Kim, M. Kjaergaard, P. Krantz, G. O. Samach, F. Yan, J. L. Yoder, K. Watanabe, T. Taniguchi, T. P. Orlando, S. Gustavsson, P. Jarillo-Herrero, and W. D. Oliver, Coherent control of a hybrid superconducting circuit made with graphene-based van der Waals heterostructures, Nat. Nanotechnol. **14**, 120 (2019).

[20] E. Portolés, S. Iwakiri, G. Zheng, P. Rickhaus, T. Taniguchi, K. Watanabe, T. Ihn, K. Ensslin, and F. K. de Vries, A tunable monolithic squid in twisted bilayer graphene, Nat. Nanotechnol. **17**, 1159 (2022).

[21] T. Yamamoto, K. Inomata, M. Watanabe, K. Matsuba, T. Miyazaki, W. D. Oliver, Y. Nakamura, and J. S. Tsai, Flux-driven Josephson parametric amplifier, Appl. Phys. Lett. **93**, 042510 (2008).

[22] M. A. Castellanos-Beltran and K. W. Lehnert, Widely tunable parametric amplifier based on a superconducting quantum interference device array resonator, Appl. Phys. Lett. **91**, 083509 (2007).

[23] M. A. Castellanos-Beltran, K. D. Irwin, G. C. Hilton, L. R. Vale, and K. W. Lehnert, Amplification and squeezing of quantum noise with a tunable Josephson metamaterial, Nat. Phys. **4**, 929 (2008).

[24] L. Zhong, E. P. Menzel, R. D. Candia, P. Eder, M. Ihmig, A. Baust, M. Haeberlein, E. Hoffmann, K. Inomata, T. Yamamoto, Y. Nakamura, E. Solano, F. Deppe, A. Marx, and R. Gross, Squeezing with a flux-driven Josephson parametric amplifier, New J. Phys. **15**, 125013 (2013).

[25] X. Zhou, V. Schmitt, P. Bertet, D. Vion, W. Wustmann, V. Shumeiko, and D. Esteve, High-gain weakly nonlinear flux-modulated Josephson parametric amplifier using a squid array, Phys. Rev. B **89**, 214517 (2014).

[26] D. J. Parker, M. Savytskyi, W. Vine, A. Laucht, T. Duty, A. Morello, A. L. Grimsmo, and J. J. Pla, Degenerate parametric amplification via three-wave mixing using kinetic inductance, Phys. Rev. Appl. **17**, 034064 (2022).

[27] T. W. Larsen, K. D. Petersson, F. Kuemmeth, T. S. Jespersen, P. Krogstrup, J. Nygård, and C. M. Marcus, Semiconductor-nanowire-based superconducting qubit, Phys. Rev. Lett. **115**, 127001 (2015).

[28] L. Casparis, M. R. Connolly, M. Kjaergaard, N. J. Pearson, A. Kringhøj, T. W. Larsen, F. Kuemmeth, T. Wang, C. Thomas, S. Gronin, G. C. Gardner, M. J. Manfra, C. M. Marcus, and K. D. Petersson, Superconducting gatemon qubit based on a proximitized two-dimensional electron gas, Nat. Nanotechnol. **13**, 915 (2018).

[29] J. G. Kroll, F. Borsoi, K. L. van der Enden, W. Uilhoorn, D. de Jong, M. Quintero-Pérez, D. J. van Woerkom, A. Bruno, S. R. Plissard, D. Car, E. P. A. M. Bakkers, M. C. Cassidy, and L. P. Kouwenhoven, Magnetic-field-resilient superconducting coplanar-waveguide resonators for hybrid circuit quantum electrodynamics experiments, Phys. Rev. Appl. **11**, 064053 (2019).

[30] L. J. Splitthoff, A. Bargerbos, L. Grünhaupt, M. Pita-Vidal, J. J. Wesdorp, Y. Liu, A. Kou, C. K. Andersen, and B. van Heck, Gate-tunable kinetic inductance in proximitized nanowires, Phys. Rev. Appl. **18**, 024074 (2022).

[31] D. Phan, J. Senior, A. Ghazaryan, M. Hatefipour, W. M. Strickland, J. Shabani, M. Serbyn, and A. P. Higginbotham, Detecting induced $p \pm ip$ pairing at the Al-InAs interface with a quantum microwave circuit, Phys. Rev. Lett. **128**, 107701 (2022).

[32] W. M. Strickland, B. H. Elfeky, Yuan JosephOConnell, W. F. Schiela, P. Yu, D. Langone, M. G. Vavilov, V. E. Manucharyan, and J. Shabani, Superconducting resonators with voltage-controlled frequency and nonlinearity, Phys. Rev. Appl. **19**, 034021 (2023).

[33] J. G. Kroll, W. Uilhoorn, K. L. van der Enden, D. de Jong, K. Watanabe, T. Taniguchi, S. Goswami, M. C. Cassidy, and L. P. Kouwenhoven, Magnetic field compatible circuit quantum electrodynamics with graphene Josephson junctions, Nat. Commun. **9**, 4615 (2018).

[34] F. E. Schmidt, M. D. Jenkins, K. Watanabe, T. Taniguchi, and G. A. Steele, A ballistic graphene superconducting microwave circuit, Nat. Commun. **9**, 4069 (2018).

[35] M. Mergenthaler, A. Nersisyan, A. Patterson, M. Esposito, A. Baumgartner, C. Schönenberger, G. A. D. Briggs, E. A. Laird, and P. J. Leek, Circuit quantum electrodynamics with carbon-nanotube-based superconducting quantum circuits, Phys. Rev. Appl. **15**, 064050 (2021).

[36] G. Butseraen, A. Ranadive, N. Aparicio, K. Rafsanjani Amin, A. Juyal, M. Esposito, K. Watanabe, T. Taniguchi, N. Roch, F. Lefloch, and J. Renard, A gate-tunable graphene Josephson parametric amplifier, Nat. Nanotechnol. **17**, 1153 (2022).

[37] J. Sarkar, K. V. Salunkhe, S. Mandal, S. Ghatak, A. H. Marchawala, I. Das, K. Watanabe, T. Taniguchi, R. Vijay, and M. M. Deshmukh, Quantum-noise-limited microwave amplification using a graphene Josephson junction, Nat. Nanotechnol. **17**, 1147 (2022).

[38] D. Phan, P. Falthansl-Scheinecker, U. Mishra, W. M. Strickland, D. Langone, J. Shabani, and A. P. Higginbotham, Gate-tunable superconductor-semiconductor parametric amplifier, Phys. Rev. Appl. **19**, 064032 (2023).

[39] M. Khalifa and J. Salfi, Nonlinearity and parametric amplification of superconducting nanowire resonators in magnetic field, Phys. Rev. Appl. **19**, 034024 (2023).

[40] M. Xu, R. Cheng, Y. Wu, G. Liu, and H. X. Tang, Magnetic field-resilient quantum-limited parametric amplifier, PRX Quantum **4**, 010322 (2023).

[41] W. Vine, M. Savytskyi, A. Vaartjes, A. Kringhøj, D. Parker, J. Slack-Smith, T. Schenkel, K. Mølmer, J. C. McCallum, B. C. Johnson, A. Morello, and J. J. Pla, In situ amplification of spin echoes within a kinetic inductance parametric amplifier, Sci. Adv. **9**, eadg1593 (2023).

[42] P. Krogstrup, N. L. B. Ziino, W. Chang, S. Albrecht, M. H. Madsen, E. Johnson, J. Nygård, C. M. Marcus, and T. S. Jespersen, Epitaxy of semiconductor-superconductor nanowires, Nat. Mater. **14**, 400 (2015).

[43] M. S. Khalil, M. J. A. Stoutimore, F. C. Wellstood, and K. D. Osborn, An analysis method for asymmetric resonator transmission applied to superconducting devices, J. Appl. Phys. **111**, 054510 (2012).

[44] S. Probst, F. B. Song, P. A. Bushev, A. V. Ustinov, and M. Weides, Efficient and robust analysis of complex scattering data under noise in microwave resonators, Rev. Sci. Instrum. **86**, 024706 (2015).

[45] A. Narla, K. M. Sliwa, M. Hatridge, S. Shankar, L. Frunzio, R. J. Schoelkopf, and M. H. Devoret, Wireless Josephson amplifier, Appl. Phys. Lett. **104**, 232605 (2014).

[46] G. Liu, T.-C. Chien, X. Cao, O. Lanes, E. Alpern, D. Pekker, and M. Hatridge, Josephson parametric converter saturation and higher order effects, Appl. Phys. Lett. **111**, 202603 (2017).

[47] V. V. Sivak, N. E. Frattini, V. R. Joshi, A. Lingenfelter, S. Shankar, and M. H. Devoret, Kerr-free three-wave mixing in superconducting quantum circuits, Phys. Rev. Appl. **11**, 054060 (2019).

[48] C. Liu, T.-C. Chien, M. Hatridge, and D. Pekker, Optimizing Josephson-ring-modulator-based Josephson parametric amplifiers via full Hamiltonian control, Phys. Rev. A **101**, 042323 (2020).

[49] C. M. Caves, Quantum limits on noise in linear amplifiers, Phys. Rev. D **26**, 1817 (1982).

[50] M. Meyer, C. Déprez, T. R. van Abswoude, I. N. Meijer, D. Liu, C.-A. Wang, S. Karwal, S. Oosterhout, F. Borsoi, A. Sammak, N. W. Hendrickx, G. Scappucci, and M. Veldhorst, Electrical control of uniformity in quantum dot devices, Nano Lett. **23**, 2522 (2023).

[51] J. Krause, C. Dickel, E. Vaal, M. Vielmetter, J. Feng, R. Bounds, G. Catelani, J. M. Fink, and Y. Ando, Magnetic field resilience of three-dimensional transmons with thin-film Al/AlO_x/Al Josephson junctions approaching 1 T, Phys. Rev. Appl. **17**, 034032 (2022).

[52] D. Rieger, S. Günzler, M. Spiecker, A. Nambisan, W. Wernsdorfer, and I. M. Pop, Fano interference in microwave resonator measurements, Phys. Rev. Appl. **20**, 014059 (2023).

[53] A. Kringhøj, T. W. Larsen, O. Erlandsson, W. Uilhoorn, J. G. Kroll, M. Hesselberg, R. P. G. McNeil, P. Krogstrup, L. Casparis, C. M. Marcus, and K. D. Petersson, Magnetic-field-compatible superconducting transmon qubit, Phys. Rev. Appl. **15**, 054001 (2021).

[54] C. K. Andersen, A. Remm, S. Lazar, S. Krinner, N. Lacroix, G. J. Norris, M. Gabureac, C. Eichler, and A. Wallraff, Repeated quantum error detection in a surface code, Nat. Phys. **16**, 875 (2020).

[55] L. J. Splitthoff, J. J. Wesdorp, M. Pita-Vidal, A. Bargerbos, and C. K. Andersen, Gate-tunable kinetic inductance parametric amplifier: Data and code (2023).

[56] H. Gehring, M. Blaicher, W. Hartmann, and W. H. P. Pernice, Python based open source design framework for integrated nanophotonic and superconducting circuitry with 2D-3D-hybrid integration, OSA Continuum **2**, 3091 (2019).

[57] R. Barends, J. Kelly, A. Megrant, D. Sank, E. Jeffrey, Y. Chen, Y. Yin, B. Chiaro, J. Mutus, C. Neill, P. O'Malley, P. Roushan, J. Wenner, T. C. White, A. N. Cleland, and J. M. Martinis, Coherent Josephson qubit suitable for scalable quantum integrated circuits, Phys. Rev. Lett. **111**, 080502 (2013).

[58] A. Kringhøj, L. Casparis, M. Hell, T. W. Larsen, F. Kuemmeth, M. Leijnse, K. Flensberg, P. Krogstrup, J. Nygård, K. D. Petersson, and C. M. Marcus, Anharmonicity of a superconducting qubit with a few-mode Josephson junction, Phys. Rev. B **97**, 060508(R) (2018).

[59] C. Macklin, K. O-Brien, D. Hover, M. E. Schwartz, V. Bolkhovsky, X. Zhang, W. D. Oliver, and I. Siddiqi, A near quantum-limited Josephson traveling-wave parametric amplifier, Science **350**, 307 (2015).

[60] C. C. Bultink, B. Tarasinski, N. Haandbæk, S. Poletto, N. Haider, D. J. Michalak, A. Bruno, and L. DiCarlo, General method for extracting the quantum efficiency of dispersive qubit readout in circuit QED, Appl. Phys. Lett. **112**, 092601 (2018).

[61] J. Y. Mutus, *et al.*, Design and characterization of a lumped element single-ended superconducting microwave parametric amplifier with on-chip flux bias line, Appl. Phys. Lett. **103**, 122602 (2013).

[62] J. Y. Mutus, T. C. White, R. Barends, Y. Chen, Z. Chen, B. Chiaro, A. Dunsworth, E. Jeffrey, J. Kelly, A. Megrant, C. Neill, P. J. J. O'Malley, P. Roushan, D. Sank, A. Vainsencher, J. Wenner, K. M. Sundqvist, A. N. Cleland, and J. M. Martinis, Strong environmental coupling in a Josephson parametric amplifier, Appl. Phys. Lett. **104**, 263513 (2014).

[63] L. Planat, R. Dassonneville, J. P. Martínez, F. Foroughi, O. Buisson, W. Hasch-Guichard, C. Naud, R. Vijay, K. Murch, and N. Roch, Understanding the saturation power of Josephson parametric amplifiers made from SQUID arrays, Phys. Rev. Appl. **11**, 034014 (2019).

[64] V. V. Sivak, S. Shankar, G. Liu, J. Aumentado, and M. H. Devoret, Josephson array-mode parametric amplifier, Phys. Rev. Appl. **13**, 024014 (2020).

[65] P. Winkel, I. Takmakov, D. Rieger, L. Planat, W. Hasch-Guichard, L. Grünhaupt, N. Maleeva, F. Foroughi, F. Henriques, K. Borisov, J. Ferrero, A. V. Ustinov, W. Wernsdorfer, N. Roch, and I. M. Pop, Nondegenerate parametric amplifiers based on dispersion-engineered Josephson-junction arrays, Phys. Rev. Appl. **13**, 024015 (2020).

[66] J. Grebel, A. Bienfait, E. Dumur, H.-S. Chang, M.-H. Chou, C. R. Conner, G. A. Peairs, R. G. Povey, Y. P. Zhong, and A. N. Cleland, Flux-pumped impedance-engineered broadband Josephson parametric amplifier, Appl. Phys. Lett. **118**, 142601 (2021).

[67] Y. Lu, W. Xu, Q. Zuo, J. Pan, X. Wei, J. Jiang, Z. Li, K. Zhang, T. Guo, S. Wang, C. Cao, H. Wang, W. Xu, G. Sun, and P. Wu, Broadband Josephson parametric amplifier using lumped-element transmission line impedance matching architecture, Appl. Phys. Lett. **120**, 082601 (2022).

[68] T. White, *et al.*, Readout of a quantum processor with high dynamic range Josephson parametric amplifiers, Appl. Phys. Lett. **122**, 014001 (2023).

[69] D. Ezenkova, D. Moskalev, N. Smirnov, A. Ivanov, A. Matanin, V. Polozov, V. Echeistov, E. Malevannaya, A. Samoylov, E. Zikiy, and I. Rodionov, Broadband SNAIL parametric amplifier with microstrip impedance transformer, Appl. Phys. Lett. **121**, 232601 (2022).

[70] B. Qing, L. B. Nguyen, X. Liu, H. Ren, W. P. Livingston, N. Goss, A. Hajr, T. Chistolini, Z. Pedramrazi, D. I. Santiago, J. Luo, and I. Siddiqi, Broadband CPW-based impedance-transformed Josephson parametric amplifier, ArXiv:2310.17084 (2023).

[71] A. Vaartjes, A. Kringhøj, W. Vine, T. Day, A. Morello, and J. J. Pla, Strong microwave squeezing above 1 T and 1 K, ArXiv:2311.07968 (2023).

[72] S. Frasca, C. Roy, G. Beaulieu, and P. Scarlino, Three-wave mixing quantum-limited kinetic inductance parametric amplifier operating at 6 T and near 1 K, ArXiv:2312.00748 (2023).